**Biophysical** Journal

rticle



# Metabolically intact nuclei are fluidized by the activity of the chromatin remodeling motor BRG1

Fitzroy J. Byfield, <sup>1,2</sup> Behnaz Eftekhari, <sup>2,3</sup> Kaeli Kaymak-Loveless, <sup>2,3</sup> Kalpana Mandal, <sup>1,2</sup> David Li, <sup>3,4</sup> Rebecca G. Wells, <sup>3,4,5</sup> Wenjun Chen, <sup>6</sup> Jasna Brujic, <sup>6</sup> Giulia Bergamaschi, <sup>7</sup> Gijs J. L. Wuite, <sup>7</sup> Alison E. Patteson, <sup>8</sup> and Paul A. Janmey <sup>1,2,5,9,\*</sup>

<sup>1</sup>Department of Physiology, University of Pennsylvania, Philadelphia, Pennsylvania; <sup>2</sup>Institute for Medicine and Engineering, University of Pennsylvania, Philadelphia, Pennsylvania; <sup>3</sup>Department of Bioengineering, University of Pennsylvania, Philadelphia, Pennsylvania; <sup>4</sup>Division of Gastroenterology and Hepatology, Department of Medicine, University of Pennsylvania, Philadelphia, Pennsylvania; <sup>5</sup>NSF Science and Technology Center for Engineering MechanoBiology, University of Pennsylvania, Philadelphia, Pennsylvania; <sup>6</sup>Center for Soft Matter Research, New York University, New York, New York, New York; <sup>7</sup>Faculty of Sciences/Division of Physics and Astronomy, Vrije Universiteit Amsterdam, De Boelelaan, Amsterdam, the Netherlands; <sup>8</sup>Department of Physics and BioInspired Institute, Syracuse University, Syracuse, New York; and <sup>9</sup>Laboratory of Magnetic Soft Materials, Department of Physics, University of Latvia, Riga, Latvia

ABSTRACT The structure and dynamics of the nucleus regulate cellular functions, with shape changes impacting cell motility. Although the nucleus is generally seen as the stiffest organelle in the cell, cells can nevertheless deform the nucleus to large strains by small mechanical stresses. Here, we show that the mechanical response of the cell nucleus exhibits active fluidization that is driven by the BRG1 motor of the SWI/SNF/BAF chromatin remodeling complex. Atomic force microscopy measurements show that the nucleus alters stiffness in response to the cell substrate stiffness, which is retained after the nucleus is isolated, and that the work of nuclear compression is mostly dissipated rather than elastically stored. Inhibiting BRG1 stiffens the nucleus and eliminates dissipation and nuclear remodeling both in isolated nuclei and in intact cells. These findings uncover a novel role of the BRG1 motor in nuclear mechanics, advancing our understanding of cell motility mechanisms.

SIGNIFICANCE Deformation of the cell's nucleus is often the limiting factor in motility through tight spaces such as the extracellular matrix. The nucleus is generally considered the stiffest organelle, and its deformation results primarily from forces generated external to it, either from the cytoskeleton or from macroscopic forces imposed on a tissue. Here, we show that the response of intact, metabolically active nuclei to compression depends on the activity of the chromatin remodeling motor BRG1, which fluidizes the nucleus and allows it to undergo large deformations even under modest mechanical stress. The significance of this work is to reveal a mechanism internal to the nucleus that enables large shape transformations without damage to chromatin or the nuclear membrane.

#### INTRODUCTION

The nucleus is generally considered the stiffest organelle of the cell (1–5), with its deformation being the limiting factor in the ability of cells to squeeze through tight spaces of the crowded cellular environment. Measurements of nuclear stiffness, usually by atomic force microscopy or microaspiration, show that apparent nuclear stiffness is weakly dependent on deformation rate and increases with increasing force, and provide values on the order of 5–10 kPa for the Young's modulus (6–8), which is significantly greater than

Submitted June 4 2024 and accepted for publication November 27 2024.

\*Correspondence: janmey@mail.med.upenn.edu

Editor: Guy Genin.

https://doi.org/10.1016/j.bpj.2024.11.3322

2024 Published by Elsevier Inc. on behalf of Biophysical Society.

the stiffness of the cell's actin-based cortex and orders of magnitude stiffer than whole suspended cells and the perinuclear or cytoplasmic volume of the cell, commonly reported to have elastic moduli on the order of 100 Pa (9–11). This model of a rigid nucleus sitting within a soft cell interior is inconsistent with the fact that cells can deform a spherical nucleus to a highly elongated shape when a cell is embedded within soft polymer networks such as those formed by a few milligrams per milliliter of collagen (12). The contractile stress generated by actomyosin in a nonmuscle cell is generally on the order of a few kilopascals at most, and even if the contractile stress were higher, the soft collagen matrix surrounding the cell, a few 100 Pa for 3 mg/mL collagen, could not support much greater stresses, even if the collagen stiffens under

deformation. A perhaps more direct demonstration that the nucleus might not be as stiff as often assumed, is the finding that lipid droplets within primary human hepatocytes that exert less than 200 Pa contractile stress are able to deform the nucleus, while retaining their own spherical shape (13,14). The high surface tension of the lipid droplet can plausibly account for the rigidity of the droplet, but the low contractile force characteristic of hepatocytes cannot account for the large local strain at the droplet-nucleus interface if the nucleus is rigid. These observations are more consistent with recent studies in which submicron-sized ferromagnetic beads were moved by magnetic fields to perform microrheology, showing that the nucleoplasmic storage (elastic) and loss (viscous) moduli are both in the range of a few hundred Pa (15).

Most studies of nuclear stiffness are made either in intact cells, where the perinuclear intermediate filament network or the overlying actin cortical network are likely to contribute to the elastic resistance even when the measurements are made directly over the nucleus, and accurately accounting for the contributions of these multilayered elastic materials is difficult. Alternatively, measurements of nuclei purified from cells after the cell's plasma membrane has been disrupted and the nuclei separated from the cell remnants by centrifugation are confounded by the fact that these nuclei have lost soluble contents by diffusion through the nuclear pores and are no longer osmotically balanced with the cytoplasm. To overcome these limitations, in this study nuclei have been prepared by centrifugation of cells attached to a glass or hydrogel surface by a mechanism in which the nucleus, which is denser than the rest of the cell, emerges from the cell body with an intact plasma membrane wrapped around it, but no cytoskeleton, ribosomes, endoplasmic reticulum, or other organelles. The space between the intact nucleus and the plasma membrane contains approximately 500 nm thickness of cytoplasm containing glycolytic enzymes capable of generating ATP. This isolated, metabolically intact nucleus, termed a karyoplast, has been studied biochemically and morphologically (16–18), but not physically.

In this study, isolated karyoplasts are characterized morphologically and deformed by atomic force microscopy using a flat cantilever to probe the full nucleus, over a wide range of deformation strains, frequencies, and timescales. Both the increased resistant force as the nucleus is deformed and the decrease in resistance as external forces are removed reveal the contributions of both viscous dissipation and elastic storage on the response of nuclei to mechanical stress. The effects of disrupting nuclear lamins, chromatin, cytoskeletal proteins, osmotic pressure, glycolysis, and nuclear motor proteins on karyoplast stiffness have been measured. The results show that the mechanical response of nuclei cannot be explained by a passive viscoelastic model but requires the activity of ATPases, consistent with the properties of an active material that can change shape in response to even small forces, if they are applied over a long time, while allowing for full recovery of the original nuclear shape when the force is removed. Inhibition of the ATPase motor RNA polymerase II has little effect on karyoplast rheology, but inhibition of the ATPase Brahma-related gene (BRG1) stiffened the karyoplast and abrogated dissipation, mimicking the effect of global ATP depletion, suggesting that movement by the Brg/Brm-associated factor (BAF) chromatin remodeling complex is essential for the active deformation of the nucleus.

#### **MATERIALS AND METHODS**

#### Cell culture

Immortalized wild-type mouse embryonic fibroblasts (mEF WT) and vimentin null fibroblasts (mEF vim null) were cultured in high-glucose DMEM (Corning Inc., Corning, NY) supplemented with 10 FBS (Sigma-Aldrich, St. Louis, MO), 0.1  $\mu$ g/mL penicillin, 0.1 mg/mL streptomycin (Mediatech, Manassas, VA), and 5 nonessential amino acids (Gibco, Carlsbad, CA). Cells were maintained at 37°C in a 5 CO<sub>2</sub> environment with saturated humidity. For all experiments, cells were used between passages 5 and 20.

# Centrifuge tube insert and polyacrylamide gel fabrication

As described previously (19), inserts for thick-walled polycarbonate ultracentrifuge tubes (32 mL capacity, Beckman Coulter, Brea, CA) were prepared by bonding air plasma-treated round 18 mm diameter glass coverslips to polydimethylsiloxane spacers (inner diameter: 13 mm; outer diameter: 20 mm; height: 3 mm). Next, inserts were functionalized by treating with (3-aminopropyl)trimethoxysilane. Polyacrylamide (PAAm) gel mixtures with Young's moduli ranging from 5 kPa (5 acrylamide, 0.15 bisacrylamide) to 22 kPa (8 acrylamide, 0.48 bis-acrylamide) were then added and polymerized under a Rain-X-treated glass coverslip. To prevent cell attachment to the uncovered glass surface, 2 agarose was added to the periphery of the gels. Inserts with PAAm gels were coated with 0.1 mg/mL collagen by first functionalizing the gel surface with sulfo-SAN-PAH and incubating with ligand overnight at 4°C. Inserts without PAAm gels underwent air-plasma treatment and were also incubated with ligand overnight. In some cases, fluorescent microspheres were added to the PAAm gels to enable traction field microscopy studies (20). Since the karyoplasts retain an intact plasma membrane, they adhere to the collagen-coated gel surface. Fig. S1 E shows the traction field immediately below adherent karyoplasts adhering to a collagen-coated polyacrylamide gel using the methods reported in (21). The very small strain fields, barely distinguishable from noise (Fig. S1 E), are consistent with gel deformation cause by the small adhesion energy of the spherical karyoplast (22), and show that the remaining cytoplasm does not spread on the surface of the hydrogel.

# Karyoplast isolation

Karyoplasts were isolated from normal or vimentin null mEFs as described previously (19) based on the methods of (23,24) with some modifications. Cells were cultured on the prepared inserts for 24–48 h before isolation of karyoplasts. Just before isolation, cells were incubated with 5  $\mu$ g/mL Hoechst (diluted in cell culture medium) for 30 min. Subsequently, samples were centrifuged at speeds ranging from 405 to 2880 × g for up to 50 min. The centrifugation was performed in DMEM supplemented with 1 FBS and 2  $\mu$ g/mL cytochalasin D at 37°C using a Beckman-Coulter Optima LE-80 K ultracentrifuge with an SW-28 rotor. To stabilize the inserts during centrifugation, polydimethylsiloxane was cured in the base of ultracentrifuge tubes to create a flat surface. During centrifugation, isolated karyoplasts were

collected in inserts coated with 0.1 mg/mL poly-D-lysine. Enucleation efficiency was assessed by imaging cells after karyoplast isolation and analyzing the percentage of cells lacking nuclei, as determined by the absence of Hoechst staining. In addition, the volume of isolated karyoplasts was calculated assuming a spherical shape based on their radii. Because previous studies have shown no differences between nuclei from normal or vimentin null mEFs (19), most experiments have been done using vimentin null mEFs, as the karyoplast preparation was more efficient, and any effects reported were always confirmed to occur in karyoplasts from normal mEFs.

# Fluorescent staining of isolated karyoplasts and cytoplasts

Freshly isolated karyoplasts were incubated with annexin V and propidium iodide for up to 24 h to determine exposure of phosphatidylserine and integrity of the plasma membrane surrounding the nuclei, respectively, using an apoptosis detection kit (Life Technologies, Carlsbad, CA; V13241). For immunostaining, both nuclei and cytoplasts were fixed with 4 paraformaldehyde for 10 min at room temperature. Samples were then permeabilized with 0.1 Triton X-100 for 5 min and incubated with 1 bovine serum albumin (BSA) for 30 min. For isolated karyoplasts, incubations were then made with lamin A/C (Cell Signaling Technologies, Danvers, MA; 4777S) and lamin B (Abcam, Cambridge, MA; ab16048) antibodies (diluted 1:500 in 1 BSA) for 1 h. For cytoplasts, incubations were made with tubulin monoclonal antibody (Bio-Rad, Hercules, CA; MCA77G) and vimentin antibody (Novus Biologicals, Centennial, CO; NB300-223) also for 1 h. Samples were then rinsed with 1 BSA and incubated for 1 h with the following fluorescently labeled secondary antibodies: goat anti-chicken IgY (Invitrogen, Waltham, MA; A11039), goat anti-mouse IgG (Invitrogen, A11029), and goat antirat IgG (Invitrogen, A11007). These antibodies were diluted 1:500 in 1 BSA. Samples were then rinsed with phosphate-buffered saline (PBS) and imaged using a 63× objective. Analysis of fluorescence intensity was performed using ImageJ.

After rinsing with PBS, samples were imaged using wide-field fluorescence microscopy with a 63× objective at the middle plane of the karyoplasts. The volume of karyoplasts imaged by single-plane epifluorescence was determined based on the radius of the karyoplasts, assuming a spherical shape. Confocal images were also acquired using an LSM 880 microscope with a 40×/1.2 water objective (Zeiss, White Plains, NY). The volume of karyoplasts imaged by confocal microscopy was calculated from Z-stack images using ImageJ. This was achieved by determining the area of each confocal slice within the Z-stack and multiplying by the height (thickness) of the corresponding slice. The volumes of all slices were then summed to provide the total volume. Analysis of mean, total fluorescence intensity, and radii of karyoplasts was performed using ImageJ. Scatterplots represent the volumes and intensities of individual karyoplasts, and the mean was calculated for each condition. A Welch's *t*-test was used to determine statistical significance based on the number of samples.

## Treatments of isolated karyoplasts

Hoechst-stained isolated karyoplasts, attached to glass coverslips unless indicated otherwise, were exposed to the following treatments: for DNA degradation experiments, karyoplasts were permeabilized with 1 digitonin and treated with 1 mg/mL DNase1 in PBS for 1 h. In treatments involving copper, karyoplasts were permeabilized with 0.1 saponin then treated with 1 mM copper sulfate in tris-buffered saline for 1 h. To investigate osmotic effects, karyoplasts were exposed to PBS, 50 PBS/50 H<sub>2</sub>O, 90 PBS/10 H<sub>2</sub>O, PBS + 100 mM NaCl, or PBS + 300 mM NaCl for 1 h. For nuclear lamin disassembly experiments, karyoplasts were treated with 90 pmol cyclin-dependent kinase-1 (CDK1) in the presence of 1 mM ATP for 1 h in suspension. ATP was added for these experiments to ensure activation of CDK1. ATP production by glycolysis was inhibited by 3-bromopyruvate (Cayman Chemical, Ann Arbor, MI;

19068). RNA polymerase was inhibited by actinomycin D (Invitrogen, A7592). The BRG1 motor of the BAF complex was inhibited by the dual BRM and BRG1 inhibitor BRM-014 (Cayman Chemical, 36138).

Following these treatments, karyoplasts were either imaged with a DM IRE2 microscope (Leica, Wetzlar, Germany) using a 63× objective or compressed using a Bruker Nanowizard 4 atomic force microscope (AFM) mounted on a Leica DMI600 fluorescence microscope.

# Fabrication of PAAm microparticles

PAAm microparticles were fabricated through inverse emulsion polymerization. For this purpose, the surfactant polysorbate 85 (Span 85, Sigma-Aldrich) was dissolved at a 2 (v/v) concentration in 200 mL of cyclohexane solvent to stabilize the spherical morphology of particles. Due to free radicals being required to initiate the polymerization of PAAm, oxygen, a free radical trap, was removed from the synthesis system by linking a nitrogen tank to the flask's rubber stopper. During the degassing process, a 10 mL PAAm solution was prepared using acrylamide, bis-acrylamide, ammonium persulfate (Sigma-Aldrich), and PBS. The final concentration of acrylamide, ammonium persulfate, and bis-acrylamide were kept constant at 4 , 0.1 (v/v), and 0.2 (v/v), respectively. Then, N,N,N,N -tetramethylethylenediamine (Thermo Fisher Scientific, Waltham, MA) was added to the PAAm solution to yield a final concentration of 0.1 (v/v). After 10 s of vortexing, the PAAm solution was added dropwise into the cyclohexane/Span 85 mixture. The stirring rate was enhanced (~1000 rpm) to make microparticles of the desired size. Once the polymerization reaction was completed (~1 h), stirring was stopped, and microparticles were allowed to settle for 30 min. The supernatant was removed, and the microbeads were washed twice with 100 ethanol and pelleted by 5 min centrifugation at  $400 \times g$ . The microbeads were then immersed overnight, in PBS, on a shaker.

### **Fabrication of fluorocarbon droplets**

A monodisperse droplet emulsion was synthesized according to a protocol adapted from (25,26), as outlined in (27). In brief, an equal volume of dimethoxydimethysilane (98 , Sigma-Aldrich) and (3,3,3-trifluoropropyl) methyldimethoxysilane (97 , Gelest, Morrisville, PA) was mixed together with deionized water at 5 vol . The mixture was homogenized by vortexing for 5 min and shaking on a shaker ( $\sim\!1000$  rpm) for 6 h. Ammonia (27 vol aqueous solution, Sigma-Aldrich) was then added at 1 vol and mixed by gently tumbling the container, and the droplets were left to grow on a rotator for 24 h. 100 mM SDS solution was added to the mixture to reach a final SDS concentration of 1 mM to prevent further growth and coalescence. The droplets were then washed three times by centrifugation with 1 mM SDS to remove ammonia and reaction byproducts, and finally stored in a 5 mM SDS solution until further use.

#### **Animal studies**

All animal work was carried out in strict accordance with the recommendations in the Guide for the Care and Use of Laboratory Animals of the National Institutes of Health. Animal protocols were approved by the Institutional Animal Care and Use Committee of the University of Pennsylvania (protocol no. 804031). ob/ob mice were obtained from the Jackson Laboratories (Bar Harbor, ME; strain no. 000632) and were housed in a temperature-controlled environment with appropriate enrichment, ad libitum feeding of standard rodent chow and water, and 12 h light/dark cycles. Euthanasia was carried out by CO<sub>2</sub> inhalation followed by exsanguination.

# Lipid droplet isolation

Lipid droplets were isolated from ob/ob mouse livers harvested at 12 weeks with a sucrose density gradient as described previously, with

Please cite this article in press as: Byfield et al., Metabolically intact nuclei are fluidized by the activity of the chromatin remodeling motor BRG1, Biophysical Journal (2025), https://doi.org/10.1016/j.bpj.2024.11.3322

Byfield et al.

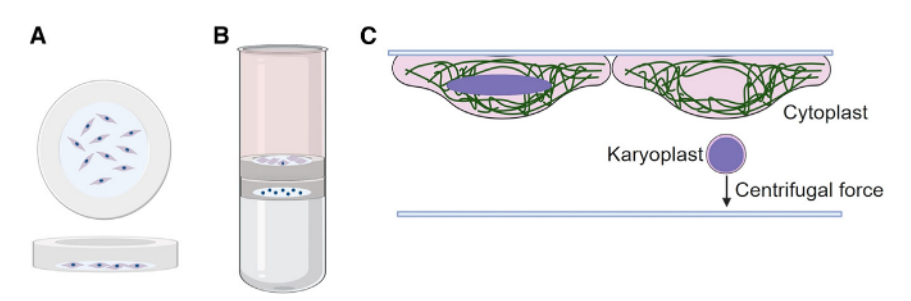


FIGURE 1 Karyoplast isolation from mouse embryo fibroblasts using centrifugation. (A) Top and side view of a centrifuge tube insert with cultured mouse embryo fibroblasts (mEFs). Inserts were made by bonding a glass coverslip to a PDMS spacer. (B) Ultracentrifuge tube containing enucleated cells in the top insert and isolated karyoplasts collected in a poly-D-lysine-coated bottom insert. PDMS was cured in the base of the ultracentrifuge tube to stabilize inserts during centrifugation. (C) Side view of a cell before and during centrifugation,

illustrating the isolation of a karyoplast based on density. Notably, the isolated karyoplast contains a nucleus that is surrounded by the donor cell's plasma membrane and a thin layer of cytoplasm.

minor modifications (28). In brief, fresh livers were minced and washed with  $1 \times DPBS$ , then homogenized in a Dounce tissue grinder (Wheaton, Millville, NJ) with 55.5 (w/v) sucrose in TE buffer (10 mM Tris-HCl [pH 7.4], 1 mM EDTA [pH 8.0]). The homogenate was centrifuged at  $1000 \times g$  for 10 min at  $4^{\circ}C$ . Eight milliliters of the supernatant was placed into a 50 mL conical, and 6 mL of 40 (w/v) sucrose in TE buffer was carefully added on top, ensuring that the two phases remained separate. Six milliliters of 25 sucrose in TE buffer, 4 mL of 10 sucrose in TE buffer, and 8 mL of TE buffer were then added in a similar fashion before centrifugation at  $2000 \times g$  at  $4^{\circ}C$  for 30 min. The top layer containing the lipid droplets was transferred using a glass pipette to a 2 mL microcentrifuge tube and washed in  $1 \times DPBS$ . All solutions contained protease and phosphatase inhibitors, used at the concentrations recommended by the manufacturer (Complete Protease Inhibitor Cocktail and PhosSTOP, Sigma-Aldrich).

#### **AFM**

AFM measurements were made with a Nanowizard 4 (Bruker, Santa Barbara, CA) mounted on a Leica DMI 6000 B microscope. Before each experiment, a calibration was made by determining the slope of the deflection of the AFM cantilever on a petri dish to determine the deflection sensitivity. Isolated karyoplasts were distinguished from cells that detached during centrifugation by a near complete overlap between bright-field images and Hoechst staining.

Karyoplasts, PAAm microparticles, fluorocarbon microparticles, and lipid droplets were compressed using tipless silicon nitride cantilevers (NP-O10, Bruker, Camarillo, CA) with a nominal spring constant of 0.35 N/m at frequencies of 0.01, 1, and 9 Hz and a maximum applied force of approximately 30 nN. All measurements were made at room temperature in PBS with a minimum of 10 samples per condition. Measurements on isolated karyoplasts and lipid droplets were made within 1–5 h of isolation.

AFM force curves were analyzed using the JPK analysis software and fit to a double-contact Hertz model for a sphere being compressed between two planes as described in Lherbette et al. using the equation: (29):

$$(F) = 2\left(\frac{3F(-\nu^2)}{4\sqrt{R_k}}\right)^{2/3}$$

where is the deformation as a function of the force F,  $\nu$  is the Poisson's ratio, E is the Young's modulus, and  $R_k$  is the radius of the karyoplast. In some cases the index of plasticity was calculated as the relative difference in the areas below the indentation and retraction curves (30).

The perinuclear region of vimentin null mEFs was indented with a 1  $\mu$ m silica bead attached to a silicon nitride cantilever (Novascan, Ames, IA) with a spring constant of 0.06 N/m. Force curves were fit to the Hertz model for a sphere contacting a homogenous elastic half space up to an indentation of 500 nm.

Scatterplots represent the apparent Young's moduli of individual karyoplasts or cells, and the mean was calculated for each condition. A Welch's *t*-test was used to determine statistical significance based on the number of samples.

#### Optical tweezers experiments

Before experiments, the microfluidic flow cell (Lumicks, Amsterdam, the Netherlands) was passivated with 0.3 casein for about 1 h, then rinsed with  $\rm H_2O$  and nuclear buffer (10 mM HEPES [pH 7.5], 2 mM MgCl<sub>2</sub>, 25 mM KCl, 250 mM sucrose, 1 mM DTT, 1 mM PMSF). Carboxylated polystyrene microspheres (3 v/v, Spherotech, Lake Forest, IL) of 4.67  $\mu$ m diameter were washed (2000 × g for 1 min) and incubated with 0.05 poly-L-lysine (Sigma-Aldrich) for 30 min at RT on a rotating Eppendorf mixer; the final pellet was resuspended in 1 mL nuclear buffer. Karyoplasts were stained with CellMask and finally diluted 1:4 in nuclear buffer (for a final volume of 150–200  $\mu$ L). For optical tweezer experiments, the karyoplast solution was flushed in channel 4, while the beads were flushed in channel 2. After catching two beads in the dual traps, the latter are moved to channel 3 (containing nuclear buffer) where the stretching experiments are performed. Additional experimental details are reported in (31).

#### **RESULTS**

The method by which karyoplasts are prepared is shown schematically in Fig. 1. Cells are cultured either on glass cover slips or hydrogel substrates for 24 h before reaching near confluence. The cover slip with or without a gel is then placed into a modified centrifuge tube containing a spacer, below which is another cover slip coated with polylysine (Fig. 1 B). Before centrifugation, the nucleus in a well spread cell is typically a highly elongated oblate ellipsoid. After centrifugation, the nucleus appears as a sphere, wrapped in a sealed plasma membrane that has separated from the rest of the cell, termed a cytoplast (Fig. 1 C).

Fig. 2 shows images of cells and their nuclei after the centrifugation process, where cells are stained for tubulin, vimentin, and chromatin. Enucleation of cells was performed using either normal mouse embryo fibroblasts or fibroblasts derived from a vimentin null mouse. Not all of the WT cells have lost their nuclei under the relatively gentle conditions of this experiment, but almost all of the cells lacking vimentin have become enucleated (Fig. 2 A). The efficiency of enucleation is shown quantitatively in Fig. 2 B. At a constant time of centrifugation (50 min), the percentage of cells that become enucleated is strongly dependent on the

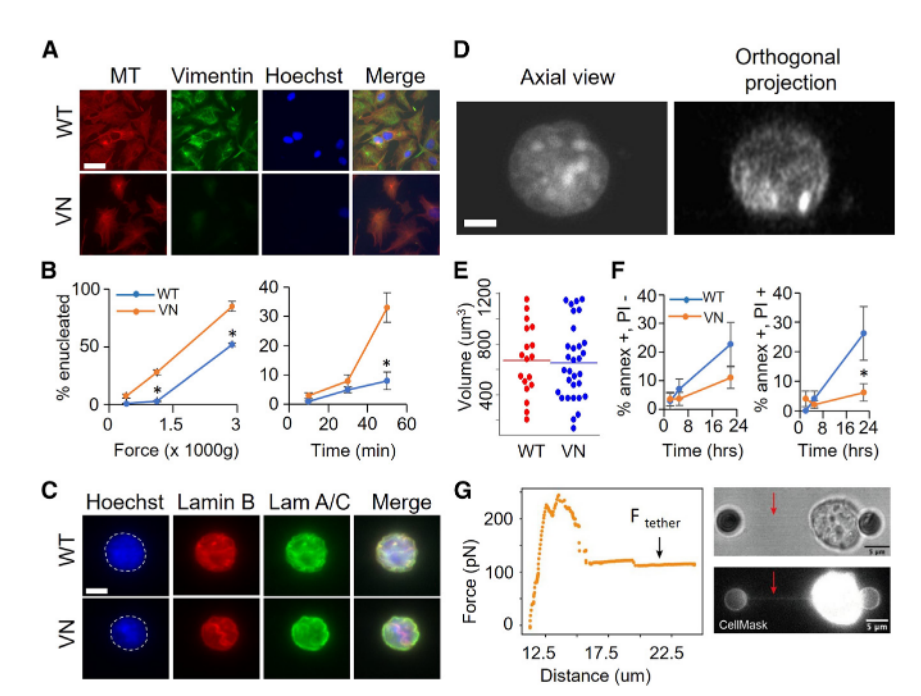


FIGURE 2 (A) Single-plane fluorescence images of WT and vimentin null mEFs after the enucleation process. Scale bar, 25 µm. (B) Analysis of enucleation rates with increasing centrifugal force for 50 min at a centrifugal force of 2880  $\times$  g from 10 to 50 min. n = 3 independent experiments standard error, p 0.05). (C) Fluores-(mean cence images of DNA (Hoechst) and Lamins A/B/C in karyoplasts isolated from WT and vim null mEFs. Scale bar, 5 µm. (D) Confocal images showing an axial view (left) and an orthogonal projection (right) of a typical karyoplast. Scale bar, 5 μm. (E) Scatterplot showing the volume of karyoplasts isolated from WT and vimentin mEFs. A minimum of 18 karyoplasts were analyzed for each cell line, and the mean was calculated. (F) Analysis of PS exposure and propidium iodide entry into isolated karyoplasts up to 22 h after isolation. n = 2 independent experiments (mean standard error, p 0.05). (G) Membrane tether being pulled from a karyoplast using optical tweezers.

centrifugal force and is significantly more efficient in vimentin null cells compared with WT fibroblasts, reaching efficiencies above 80 with a few 1000 × g centrifugal force. At a constant centrifugal force, the efficiency of enucleation is strongly time dependent and again more efficient for vimentin null than WT cells. A large fraction of nuclei can be pulled out of a cell within 50 min after the centrifugation has started. The appearance of the karyoplasts after their separation from the cells is shown in Fig. 2 C. The nuclear lamina is wrinkled, as the spherical nucleus of the karyoplast emerges from a flattened nucleus in the adherent cell and its area/volume ratio decreases, and there are no detectable differences between nuclei isolated from normal or vimentin null fibroblasts. Fig. 2 D shows confocal imaging, confirming that karyoplasts are spheres, with a small flat contact area where they adhere to the substrate. Fig. 2 E shows that the volumes of the spherical nuclei are indistinguishable between WT and vimentin null cells and are similar to the values of the nuclei measured by light-sheet microscopy in intact cells of the same cell types (32). The variance of karyoplast volumes parallels the variance of whole-cell volumes (32,33) and suggests that there is not a strong selection bias to remove either small or large nuclei, consistent with the ability to remove nuclei from nearly all of the cells, at least for vimentin null fibroblasts.

The integrity of the plasma membrane is largely maintained in the karyoplasts after centrifugation, as shown in Fig. 2 F. Only a small fraction of the karyoplasts stain positive for annexin V, a marker that reveals the presence of phosphatidyl serine on the external leaflet of the plasma membrane, a sign that the cell or karyoplast has either un-

dergone membrane disruption or has lost metabolic activity and the ability to maintain the enzymatic activity responsible for lipid bilayer asymmetry. We also find only a small fraction of propidium iodide-positive karyoplasts, which indicates disrupted plasma membranes, allowing the dye to enter the nucleus and stain the chromatin. Fig. 2 F shows that karyoplasts remain largely annexin V negative for many hours after their isolation, especially for those removed from vimentin null cells. Ninety percent of the karyoplasts prepared from these cells maintain plasma membrane integrity and asymmetry for at least 23 h after their isolation, during which time the rheological measurements of this study are done.

Like the nuclear lamina, the plasma membrane also has excess surface area beyond the minimum to surround the spherical nucleus, because membrane tethers can be pulled from it with forces similar to those required to pull tethers from an intact cell. To demonstrate this, we performed dual-trap optical tweezers experiments using two polylysine-coated beads to manipulate karyoplasts. This method facilitates localized force application directly onto the karyoplast membrane and allows precise control over bead attachment. When pulling on karyoplasts, we observed a distinct drop in the force data (Fig. 2 G) followed by a plateau F<sub>tether</sub>, a characteristic signature observed during tether pulling from cells (34,35). Simultaneously, fluorescence imaging of the karyoplast membrane, achieved by staining the karyoplasts with CellMask enabled real-time visualization of membrane stretching. Interestingly, we observed fluorescence along the tethers being pulled (Fig. 2 G), indicating that their origin is the plasma membrane of the karyoplasts.

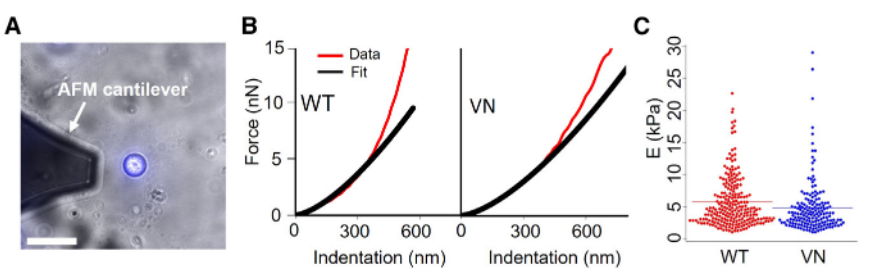


FIGURE 3 Mechanical properties of karyoplasts isolated from WT and vimentin null mEFs. (A) AFM cantilever positioned next to a karyoplast isolated from a vimentin null fibroblast attached to a poly-D-lysine coated surface. Scale bar, 20  $\mu$ m. (B) Force versus indentation curves for karyoplasts isolated from WT and vimentin null mEFs fitted to the Hertz model. (C) Scatterplot representation showing the Young's moduli of individual karyoplasts isolated from each cell

type. A minimum of 180 karyoplasts were analyzed for each cell line, and the mean was calculated. At least 4 independent experiments were performed.

The rheological response of karyoplasts as measured by AFM is shown in Fig. 3. To perform AFM studies, we use a large tipless silicon nitride cantilever that can make wide contact across the upper surface area of the karyoplast. The AFM cantilever is lowered onto the karyoplast, and the resulting force as the entire karyoplast is deformed is plotted against the change in karyoplast height, as shown in Fig. 3 B. Similar to the finding that the appearance and size of nuclei are similar when prepared from WT or vimentin null cells, the apparent stiffness is also similar. An apparent Young's modulus can be calculated from appropriate fitting to the force deformation curves (materials and methods) and reveals an apparent Young's modulus between 5 and 6 kPa for both WT and vimentin null cells.

To determine which structures within the nucleus are responsible for its mechanical properties, karyoplasts have been treated with various agents to disrupt their membranes, the nuclear lamina, or chromatin. Chromatin structure was altered either by digesting DNA with DNase1 or condensing it with copper ions. Since the plasma membrane is impermeable to large solutes, it was locally destabilized using digitonin, which clusters cholesterol and opens pores in the plasma membrane bilayer, but has no discernable effect on the nuclear membrane, which contains much less cholesterol (36) and the low amount of cholesterol that is seen in the nuclear membrane is limited to the outer nuclear membrane, leaving the inner bilayer cholesterol poor (37). Permeabilization of the plasma membrane by digitonin has little effect on the overall nuclear morphology, as shown in Fig. 4, A and B, although there appeared to be effects on the intensity of Hoechst staining (Fig. S1 F). However, when DNase1 was added to the medium containing the karyoplasts and allowed to diffuse within the nucleus there was an abrupt change in nuclear size and stiffness. The loss of Hoechst staining as shown in Fig. 4 A confirms that much of the DNA was removed from the karyoplast, and this perturbation led to a change in nuclear volume, dropping from  $\sim 700$  to 250  $\mu$ m<sup>3</sup> (Fig. 4 B). Along with the change in volume, the remaining karyoplasts became much stiffer, increasing in apparent Young's modulus to nearly 15 kPa. Perturbing the chromatin without removing DNA was examined by altering DNA with copper, which had a very different effect on nuclear morphology and stiffness. Copper ions bind tightly to DNA, altering its helical structure and are associated with neurodegenerative and other disease states (38,39). Excess copper has also been reported to associate more with heterochromatin than euchromatin in nuclei (40). As Fig. 4, C and D show, copper caused the DNA staining to become somewhat more clustered in the center of the karyoplast and increased apparent staining of lamin B, presumably because the condensation of chromatin allowed better access of the anti-lamin B antibody to the nuclear lamina. These perturbations did not change karyoplast volume but approximately doubled the stiffness of the karyoplasts.

Next, we examined the role of the nuclear lamina on karyoplast stiffness. Fig. 5 A shows nuclei before and after treatment with CDK1, a kinase that phosphorylates nuclear lamins and leads to their disassembly from the nuclear membrane. The loss of lamin staining after CDK1 is quantified in Fig. 5 B. Despite loss of the lamin network, the volume of the karyoplasts was unchanged (Fig. 5 C). We also confirm a previous report that nuclei in karyoplasts from normal and vimentin null cells have the same volume (19) (Fig. 5 C). In contrast to the large effect of destabilizing nuclear lamins on local high curvature deformations of the nuclear membrane or when nuclei are stretched as cells traverse narrow spaces (41-43), Fig. 5 D shows that the apparent Young's modulus decreases by less than 50 when the nuclear lamina is disrupted. Excluding one value for controls which was >3 times the standard deviation away from the mean, the mean value of apparent Young's modulus for normal karyoplasts is 3.3 0.9 kPa (mean and standard deviation; n = 18) and 2.6 1.0 kPa: n = 21 after treatment with CDK1, with p = 0.03.

Similarly, treatment with cytochalasin, an inhibitor of cellular actin polymerization or azide, an inhibitor of ATP generation by mitochondria, had negligible effect on nuclear stiffness or morphology. These effects are expected since the cytoplasmic cytoskeleton and mitochondria are essentially absent from the plasma membrane-coated nuclei that constitute karyoplasts (Fig. S1 A).

In contrast to the relatively small effects of inhibiting the nuclear lamina or the cytoskeleton, osmotic stresses had large effects on both the volume and stiffness of karyoplasts. Fig. 6 A shows how the volume of karyoplasts is altered under hyperosmotic pressure caused by increasing the salt concentration in the surrounding medium, or by hypoosmotic

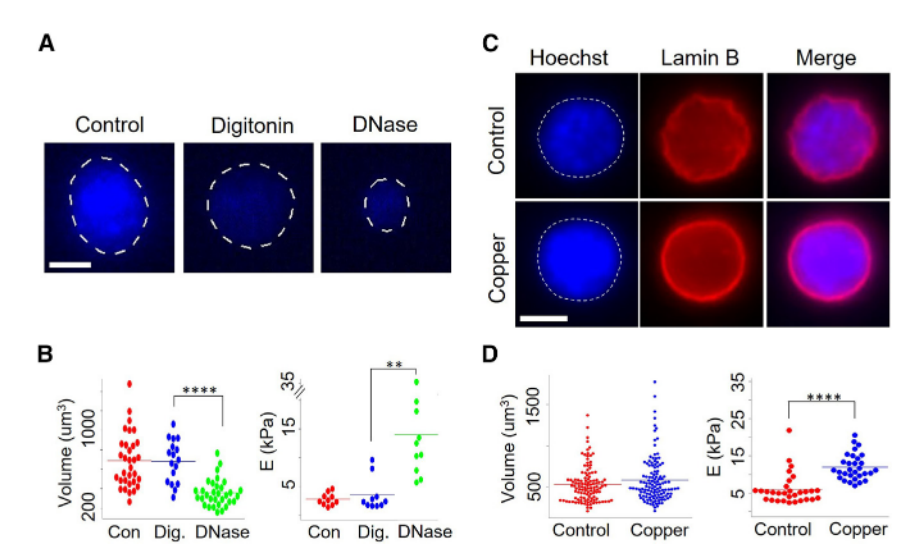


FIGURE 4 Volume and mechanical properties of karyoplasts treated with DNase I or copper. (A) Hoechst staining of isolated karyoplasts from vimentin null mEFs under control, digitonin, and digitonin + DNase treatments. Scale bar, 10 μm. (B) Scatterplots illustrating the volume (digitonin versus DNase, p = 0.00001) and Young's moduli (digitonin versus DNase, p = 0.005) of individual karyoplasts corresponding to the treatments in (A). A minimum of 10 karyoplasts were analyzed for each condition, and the mean was calculated. n =2 independent experiments. (C) Fluorescent images of karyoplasts treated with 1 mM copper sulfate. Scale bar, 10 µm. (D) Scatterplots representing the volume and Young's moduli (control versus copper treatment, p 0.00001) of individual karyoplasts corresponding to the treatments in (C). A minimum of 40 karyoplasts were analyzed for each condition, and the mean calculated. n = 4 independent experiments.

medium. The volume of the karyoplast decreases by less under an osmotic stress generated by adding 300 mM NaCl or 600 mOsM to PBS, which is estimated from van 't Hoff's equation to correspond to > 200 kPa pressure, but the volume increases by nearly a factor of 3 when the osmotic pressure of the medium is decreased by dilution of PBS with water, decreasing the osmolarity by less than 150 mM (Fig. 6 B). Along with these changes in nuclear volume, both hyper- and hypoosmotic stresses had a large effect on the apparent Young's modulus of the karyoplasts as shown in Fig. 6 C and D (10 PBS versus PBS, p = 0.0009; PBS versus + 300 mM NaCl, p = 0.02). Hypoosmotic swelling, which led to a nearly threefold change in volume, also led to approximately a threefold decrease in elastic modulus. In contrast, the relatively small change in volume under hyperosmotic conditions led to a seven times increase in elastic modulus, consistent with the idea that the nucleus can accommodate relatively large volume changes by increasing water content but cannot decrease volume by the same amount because of the large solid content held within the nuclear membrane even if it remains mostly water.

The apparent Young's moduli of nuclei and cells measured by AFM is commonly calculated from the increasing force applied to the AFM cantilever as it is pressed into the cell or the karyoplast. Fitting these force-indentation curves to a Hertz relation assumes a linear elastic continuous material and yields an apparent Young's modulus, but even an excellent fit of the Hertz relation to the force-displacement data does not guarantee that the cell or the nucleus is a linear elastic object. Fig. 7 A shows that when the AFM cantilever is first pushed into the karyoplast and then pulled back there is a large

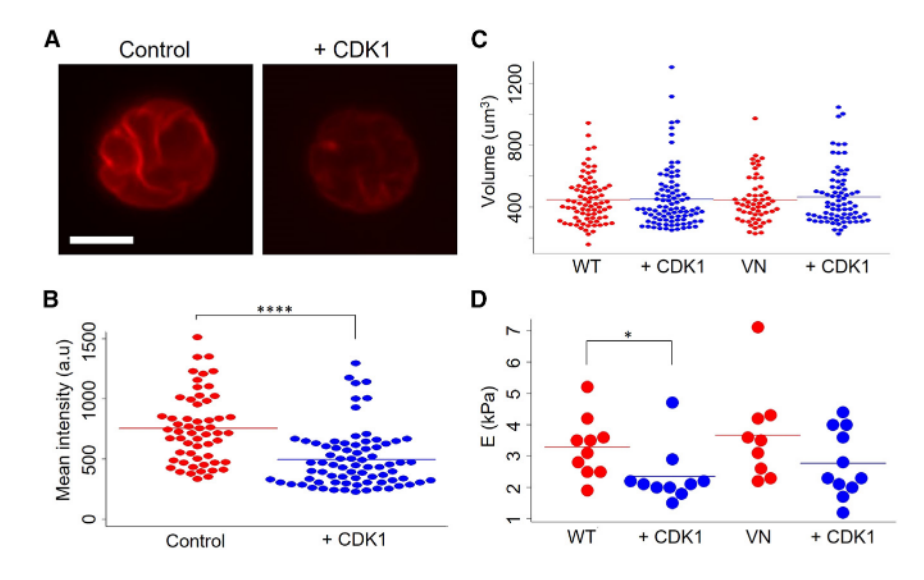


FIGURE 5 Volume and mechanical properties of karyoplasts treated with cyclin-dependent kinase1 (CDK1). (A) Lamin B staining of isolated karyoplasts treated with 90 pmol CDK1 for 90 min. Scale bar, 10  $\mu$ m. (B) Scatterplot illustrating the mean fluorescent intensity of individual isolated karyoplasts after treatment with CDK1. A minimum of 60 karyoplasts were analyzed for each condition, and the mean calculated. p = 0.001. n = 2 independent experiments. (C) Scatterplot representing the volume of individual karyoplasts isolated from WT and VN mEFs with and without CDK1 treatment. A minimum of 60 karyoplasts were analyzed for each condition, and the mean was calculated. n=2 independent experiments. (D) Scatterplot representing the Young's moduli of individual karyoplasts isolated from WT and VN mEFs with and without CDK1 treatment (WT versus WT + CDK1, p = 0.04). A minimum of 10 karyoplasts were analyzed for each condition, and the mean calculated.

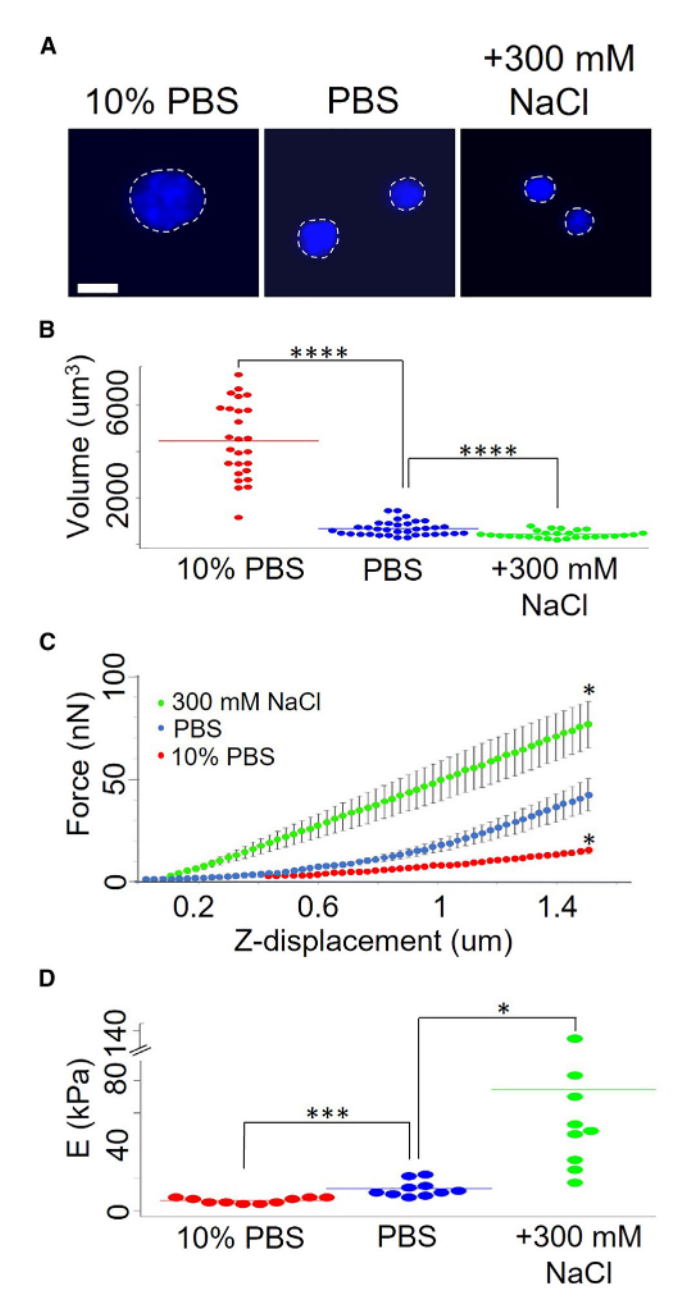


FIGURE 6 Volume changes and mechanical response of karyoplasts to osmolarity. (A) Hoechst staining of karyoplasts in hypo- (10 PBS + 90 ddH<sub>2</sub>O) and hyperosmotic (PBS + 300 mM NaCl) solutions for 1 h). Scale bar, 10  $\mu$ m. (B) Scatterplots illustrating the volume (10 PBS versus PBS, p=0.00001; PBS versus + 300 mM NaCl, p=0.00008). (C) AFM force curves of karyoplast compression after changes in osmolarity. A minimum of 10 karyoplasts were analyzed for each condition (mean—standard error, p=0.05). (D) Scatterplots showing the Young's moduli (10 PBS versus PBS, p=0.0009; PBS versus + 300 mM NaCl, p=0.02) of karyoplasts placed in hypo- and hyperosmotic solutions.

difference in the force-displacement curves during indentation and recovery. This difference does not result from any damage or permanent change to the nucleus since repeated measurements of indentation and relaxation yield similar force-displacement curves. The repeatability of multiple deformations together with the extensive dissipation suggests an elastic structure acting in parallel with the highly dissipative material. As the height of the karyoplast decreases during compression its projected area increases, again nearly identically, during each compression cycle (Fig. 7 B) confirming that volume is conserved during these large deformations. At maximum, the compressive stress is near 50, but the area does not reach the value seen for the nuclei in intact cells (32), showing that the cell on a rigid surface compresses its own nucleus more than can be done with the AFM at 50 strain. The reversibility of the indentation and the lack of permanent change is confirmed by the nearly perfect superposition of a decrease in nuclear height and an increase in the projected area (Fig. 7 C, top) consistent with a volumeconserving deformation that can be repeated with very little change in the relation between nuclear height and projected area. In contrast to the simultaneous change in karyoplast height and area, there is a significant lag between the vertical compression of the karyoplast and the development of force pushing on the AFM cantilever. Fig. 7 C, bottom, shows that the area increases more rapidly than the development of force during the compression phase but also continues to decrease even after the resisting force has relaxed nearly to the baseline. This lag between deformation and force, consistent with a highly dissipative material, is nevertheless reversible when the deformation is done again a few seconds after an initial indentation and recovery have occurred. Fig. 7 D shows that the hysteresis in the force-displacement curves is not the result of a simple viscous element because even though the dissipation is very large it is only weakly rate dependent over nearly three orders of magnitude, and the measured Young's modulus is also nearly independent of frequency.

The possibility that the hysteresis between indentation and recovery might be an artifact of the AFM measurement, possibly due to unrecognized adhesion of the karyoplast to the substrate or the cantilever, is countered by similar experiments done on three different kinds of small spherical objects. Fig. 7 *E* shows that the force-indentation of a polyacrylamide sphere made by microemulsion is nearly purely elastic, as expected from the simple elastomeric crosslinked polyacrylamide gel. Fig. 7 *E* shows similarly that lipid droplets purified from liver or droplets formed by fluorocarbon oil, in which the elastic resistance comes entirely from surface tension that cannot relax during deformation, show a nearly perfect correspondence between indentation and recovery during an AFM measurement similar to that applied to the karyoplast.

The elastic modulus of the karyoplast is not simply related to nuclear volume nor to the amount of chromatin, as shown in Fig. 8. Karyoplasts were isolated from cells cultured on glass or polyacrylamide substrates with elastic moduli of 22 or 5 kPa, which mimic the mechanical properties of soft tissues in which fibroblasts occur *in vivo*. The structures of cells, cytoplasts, and karyoplasts prepared on the three different substrates are shown in Fig. 8 A and confirm that

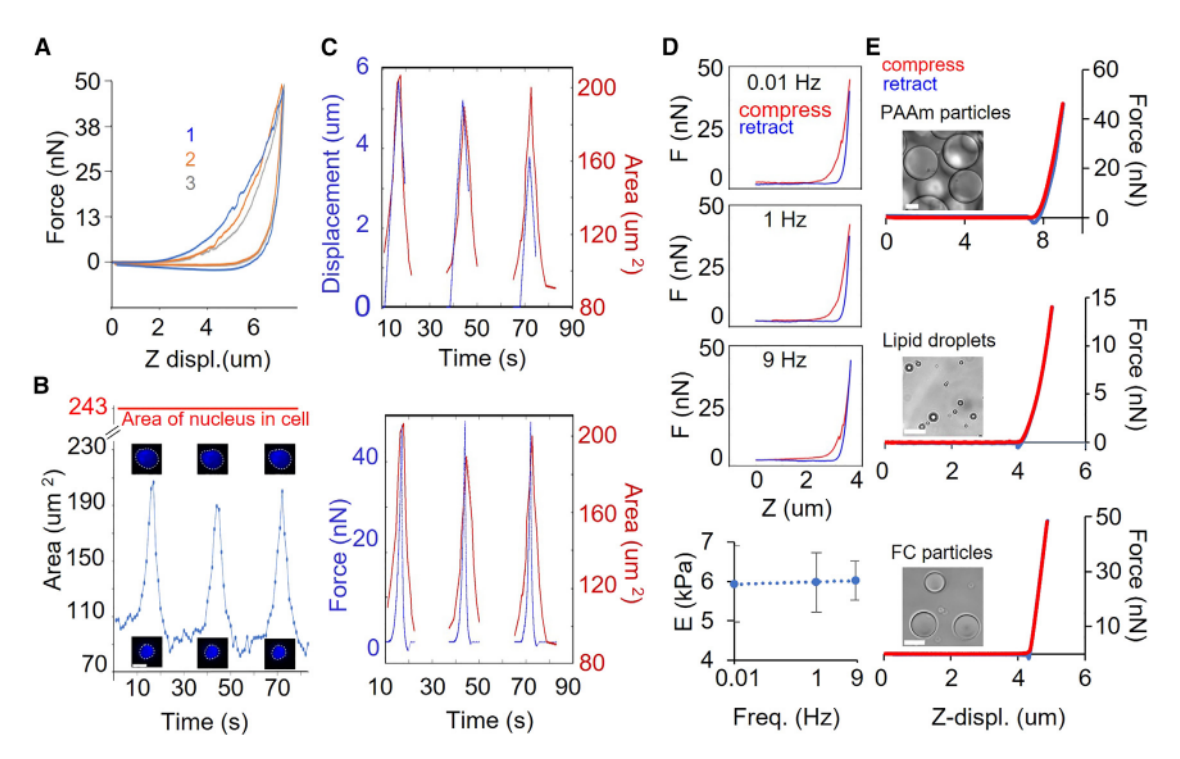


FIGURE 7 Comparison of dissipation during compression of karyoplasts and spherical microparticles. (A) AFM force curves showing consecutive compressions of a karyoplast at 0.1 Hz. The AFM cantilever was positioned to compress the entire karyoplast for consecutive measurements. (B) Area analysis of karyoplast imaged during consecutive compressions. Scale bar, 10 μm. (C) Comparison of karyoplast area change, deformation, and applied force over time for three consecutive compressions of a karyoplast. (D) AFM compression curves for a karyoplast compressed at rates of 0.01, 1, and 9 Hz and a plot of Young's modulus versus frequency. (E) AFM compression of PAAm microparticles, lipid droplets, and fluorocarbon particles compressed at 1 Hz. Scale bars, 20 µm.

nuclei can be removed from cells on each of the mechanically distinct substrates. After their removal from the cells, the karyoplasts look approximately similar, independent of the substrate stiffness (Fig. 8 B). Even hours after isolation of the nuclei from cells under these mechanical conditions, the volumes of the karyoplasts remain constant and indistinguishable from each other (Fig. 8 C), but the apparent elastic moduli of the karyoplasts are significantly different. Karyoplasts isolated from cells cultured on soft substrates had apparent Young's moduli less than 30 of those isolated from cells cultured on glass (Fig. 8 D), even though the volumes of their nuclei and presumably the amount of chromatin within them is the same (Fig. 8 C). The hysteresis between compression and recovery is large in all cases and shows a trend toward more dissipation in nuclei isolated from cells on soft substrates (Fig. 8 E).

The very weak dependence of the apparent Young's modulus on frequency and the high extent of rate independent dissipation shown in Fig. 7 suggest that the mechanical dissipation occurring during deformation of the nucleus might result from an active process, rather than simple viscoelasticity. This possibility was tested by global inactivation of ATP-dependent motor proteins by treating the isolated karyoplasts with the glycolysis inhibitor 3-bromopyruvate. Inhibiting ATP production from glycolysis has a large effect on both the elastic modulus and the amount of dissipation when a nucleus is compressed. Fig. 9 A shows that the hexokinase inhibitor 3-bromopyruvate produces an insignificant effect or possibly a small increase in the volume of karyoplasts, but Fig. 9 B shows that it has a large effect on both stiffness and the amount of dissipation when nuclei are compressed. The apparent Young's modulus increases by nearly a factor of 4 and the hysteresis between indentation and recovery is nearly eliminated.

The possibility that the dissipation is due to an active process driven by a chromatin remodeling enzyme or other motor protein was tested using specific inhibitors. The stiffening effect of ATP depletion was almost completely recapitulated by inhibition of a single ATPase in the nucleus, the BRG1 motor that drives chromatin reorganization by the BAF or SWI/SNF complex (44). Inhibiting BRG1 slightly increases nuclear volume (Fig. 9 C), but it strongly increases the apparent Young's modulus and decreases dissipation (Fig. 9 D) in a concentration dependent manner (Fig. 9 E), suggesting that the energy dissipation resulting from nuclear displacement is largely driven by active motions of chromatin.

To test whether mechanical effects of BRG1 inhibition can also alter nuclear rheology in the intact cell, adherent fibroblasts were treated with similar doses of the BRG1 inhibitor. After a few hours of incubation, the fibroblasts remained attached to the substrate and looked similar to

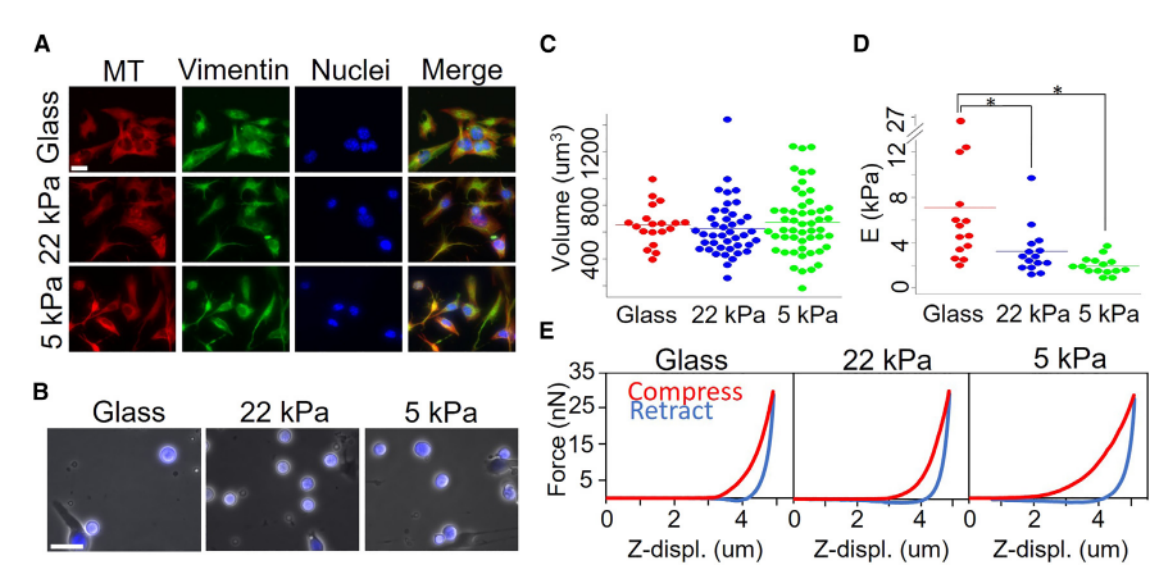


FIGURE 8 (A) Fluorescence images of mEF WT cells and cytoplasts on collagen-coated glass, 22 kPa PAAm and 5 kPa PAAm gels showing microtubules (MT) stained with anti-tubulin antibodies, vimentin stained with anti-vim antibodies and DNA stained with Hoechst. Scale bar, 20  $\mu$ m. (B) Hoechst staining of karyoplasts isolated from mEFs cultured on glass, 22 kPa, and 5 kPa PAAm gels. Scale bar, 20  $\mu$ m. (C) Scatterplots illustrating volume of karyoplasts shown in (B) and (D) Young's moduli of individual karyoplast isolated from mEFs grown on substrates of varying stiffness (glass versus 22 kPa, p = 0.05, glass versus 5 kPa, p = 0.01). (E) AFM force curves for karyoplasts isolated from cells grown on substrates of varying stiffness. A minimum of 13 karyoplasts were analyzed for each condition, and the mean calculated. At least 2 independent experiments were performed.

those of the control uninhibited cells as shown in Fig. 9 F. However, when subjected to centrifugal forces needed to pull the nuclei out of the cell to create a karyoplast, cells in which BRG1 was inhibited were unable to undergo this morphological transformation. Fig. 9 G shows that, under conditions at which nearly 60 of control cells become enucleated, only 10 of nuclei could be removed from cells that had inactive BRG1. This effect does not directly probe cellular nucleus mechanics, but it does suggest that the transition of the flat nucleus to the sphere that emerges in the karyoplast is prevented when BRG1 is inhibited. Additional experiments show that BRG1 inhibition does not change the cortical cell stiffness (Fig. S1 K) ruling out the possibility that lower enucleation rates could be due to cell stiffening.

Another perturbation of the karyoplast that stiffens it and eliminates dissipation is dissolution of chromatin by DNase I. Fig. 4 shows how DNase I activity shrinks the nucleus and increases its Young's modulus, and Fig. S1 B shows that coincident with nuclear stiffening is loss of dissipation. Most other perturbations of the karyoplast led to either no change or an increase in the amount of dissipation, whether or not they altered the apparent Young's modulus. Fig. S1 H shows that disassembly of the nuclear lamina, which makes the nuclei somewhat softer, sometimes led to a small but statistically insignificant change in the hysteresis between indentation and recovery. Inhibition of RNA polymerase by actinomycin D had only a modest effect on nuclear volume (Fig. S1 C) and a small softening effect on karyoplasts, with possibly an increase in dissipation (Fig. S1). These results suggest that the energy dissipation is largely independent of the nuclear lamina but dependent on DNA and some element that actively promotes chromatin movement.

# **DISCUSSION**

Formation of karyoplasts, in which an intact nucleus has been in continuous chemical equilibrium with the cytosol and in which large elastic structures of the cytoskeleton and cytoplasmic organelles have been removed while retaining an intact plasma membrane and continuous ATP production, permits mechanical investigations of nuclear structure and mechanics without confounding factors from the rest of the cell. Removal of nuclei from the cell by gentle centrifugation relaxes the stress that the cytoskeleton exerts on the nucleus and retains the chemical composition of the nucleus under variable physical conditions caused by such factors as substrate stiffness without the capacity to exchange nuclear contents with the rest of the cell. Our measurements of metabolically active nuclei within the karyoplast reveal some novel aspects of nuclear structure and mechanical properties. The major finding is that a large fraction of the work done to compress the nucleus is dissipated rather than elastically stored. This dissipation is not likely the result of viscoelasticity but rather requires ATP and the activity of the chromatin remodeling complex BAF (SWI/ SNF), driven by the ATPase BRG1. It might be possible to construct some kind of soft glassy model that could fit the frequency independence of rheological data, but there is no reason to think this would require ATP or the BRG1 motor. The simplest interpretation is by analogy with the

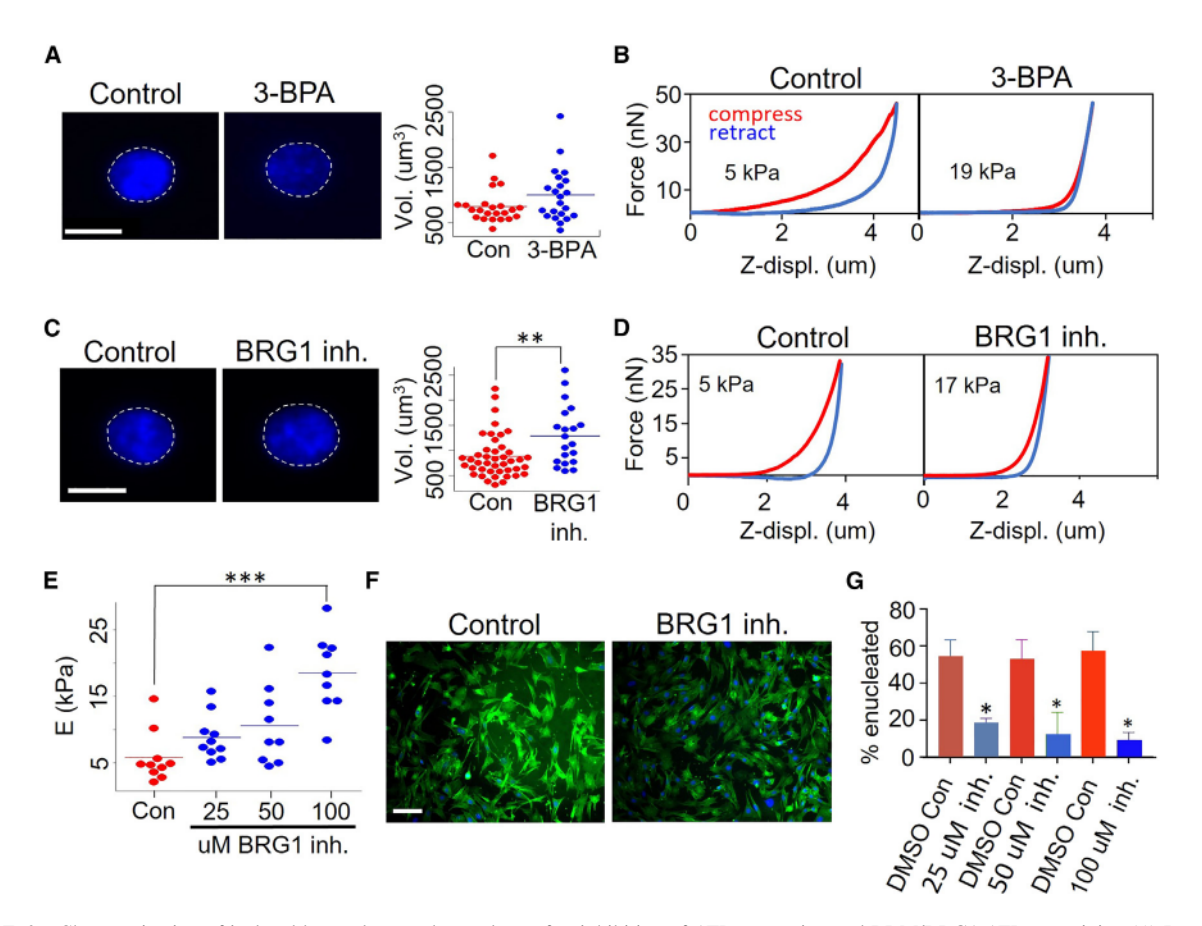


FIGURE 9 Characterization of isolated karyoplasts and cytoplasts after inhibition of ATP generation and BRM/BRG1 ATPase activity. (A) Images and volume analysis of Hoechst-stained karyoplasts incubated with 100 µM 3-bromopyruvic acid for 2 h. A minimum of 10 karyoplasts were analyzed for each condition, and the mean was calculated. Scale bar, 10 µm. (B) AFM compression curves of isolated karyoplasts treated with 3-bromopyruvic acid compared with DMSO control. (C) Images and volume analysis of isolated karyoplasts treated with 100 µM BRM/BRG1 inhibitor for 2 h (control versus BRM/BRG1 inhibitor, p = 0.009). Scale bar, 10  $\mu$ m. A minimum of 10 karyoplasts were analyzed for each condition, and the mean was calculated. (D) AFM compression curves for karyoplasts treated with 50 µM BRM/BRG1 inhibitor compared with DMSO control. (E) Scatterplot illustrating the Young's moduli of individual karyoplasts after treatment with increasing concentrations of BRM/BRG1 inhibitor (control versus 100 µM BRM/BRG1 inhibitor, p (F) F-Actin (green) and Hoechst (blue) staining of control and BRM/BRG1 inhibitor treated vim null MEFs. Images were taken after the enucleation procedure. Scale bar, 50 µm. (G) Analysis of enucleation efficiency after treatment with BRM/BRG1 inhibitor. At least 2 independent experiments were performed.

crowded cytoplasm of the bacterium, which solidifies unless enzymatic activity creates motions to fluidize it (45,46).

As reported earlier, nuclei from normal and vimentin null cells produce indistinguishable karyoplasts (19), but their formation is more efficient from cells lacking the perinuclear vimentin network. The volumes of karyoplasts are also indistinguishable from those of the intact cells from which they are prepared (32), suggesting that the osmotic balances that control nuclear size in the cell are maintained in the karyoplast. Once isolated, the karyoplast volume is strongly dependent on osmotic conditions. Numerous recent studies have shown how nuclear and cell volumes are altered by osmotic pressures caused by changes in solvent concentration (33,47-49), and that nuclei become stiffer when they are osmotically compressed (50). Consistent with these studies, the results in Fig. 6 show that nuclear volume can be increased strongly under hypoosmotic conditions but decreased only to a limited extent in hyperosmotic conditions, presumably because the solute content within the nucleus is near the point at which the activity of water is far from that in a dilute solution (47).

Numerous studies indicate that both the nuclear lamina and chromatin configuration play significant roles in shaping and maintaining the rigidity of the nucleus (51). Studies of isolated nuclei using pipette stretchers indicate that the level of euchromatin and heterochromatin mediates nuclear stiffness at relatively small strain, while at larger extensions lamin A/C control stiffening of the nucleus (52) with loss of lamin A/C decreasing stiffness by 36 large strains.

Measurements with micropipette aspiration also show an approximately 50 decrease in nuclear stiffness with lamin A/C knockdown (53). Furthermore, disruption of nuclear lamins increases nuclear deformations and can lead to

nuclear abnormalities, such as blebbing and nuclear envelope rupture (54). Our results of AFM compression of isolated nuclei show similarly a modest decrease in nuclear stiffness upon treatment with CDK1, which disassembles the nuclear lamina, and that the loss of lamina does not alter the degree of dissipation during nuclear compression (Figs. 5 and S1 H). The relatively small effect of disrupting the nuclear lamina is also consistent with previous studies showing that deformation to strains below 40 are dominated by the nuclear interior with the lamina dominating at larger strains (52). In addition to the nuclear lamins, our study highlights a significant role of nuclear activity and the BRG1 motor of the SWI/SNF complex in mediating nuclear stiffness.

Perhaps the most striking rheological characteristics of karyoplasts are the high degree of dissipation when they are deformed to large extents, the reversibility when compressed to strains greater than 50 , and the dependence of mechanical dissipation on the generation of ATP and the activity of intranuclear motor proteins. The partly fluid nature of the nucleus has been shown previously, for example in striking images of nuclei being pulled into microcapillaries (53) and by measurements of chromatin deformation by a ferromagnetic bead in a magnetic field gradient, which also emphasized the fluidity of the nucleus (55). The ability of the nucleus to flow in response to an external stress does not appear to be the result only of a high passive viscosity, but rather is due to active fluidization of the dense intranuclear core. This fluid nature of the karyoplast disappears when DNA is digested, glycolysis is prevented, or when the BRG1 motor of the SWI/SNF complex is inhibited (Fig. 9).

The high degree of karyoplast stiffening upon ATP depletion is closely paralleled by recent AFM studies of nuclear stiffness in intact cells before and after permeabilization. In the intact cell, the nuclear region has an apparent Young's modulus of 5 kPa, but when the nucleus is exposed to the medium by detergent permeabilization of the cell and nuclear membranes, the elastic modulus rises to 22 kPa (7), very similar to the values shown in Fig. 9. Other studies, however, report that the nucleus within the cell is stiffer than the isolated nucleus, because of cell-generated stresses that deform the nucleus and stiffen it by pre-tension (8).

The BRG1-containing chromatin remodeling complexes SWI/SNF or BAF have structural and dynamic properties consistent with their ability to fluidize the nucleus. These complexes can move chromatin or naked DNA at rates of 50 base pairs per second (bp/s) with a step size of 2 bp (0.7 nm) (56,57), implying that the turnover rate of the motor is > 25 Hz, which is faster than the rates of deformation accessible to the AFM (Fig. 7), and therefore consistent with the finding that, although nuclear deformation is largely dissipative, it is not rate dependent over the range of our measurements. The force developed by this motor is also remarkably high, 12 nN (57), enabling it to make large

movements in the dense environment of the nucleus. Previous studies show that disruption of BRG1 activity alters nuclear shape (58,59), and the continuous activity of the BRG1-driven BAF/SWI/SNF complex is required for access of transcription factors to their DNA targets (60–62).

The data presented here show that fluidization of the nucleus is eliminated when the BRG1 motor is inhibited, but other structures within the nucleus might also be important in determining both the Young's modulus and the degree of dissipation. When karyoplasts are isolated from cells cultured on substrates with different stiffnesses, they retain very different rheological properties even long after their isolation from the cell. One well-documented difference in nuclear structure that depends on substrate stiffness is the trafficking of the transcription regulatory proteins YAP and TAZ into the nucleus. Whether alterations in transcription profiles are sufficient to change nuclear stiffness is not known. However, another structure that was recently shown to change strongly with substrate stiffness is the amount of polymerized nuclear actin (63). Networks of nuclear actin filaments form when cells are cultured on stiff substrates but only amorphous structures of similar concentrations of actin are seen in the nucleus of cells on soft substrates. The role of actin and myosin motors in the nucleus is much less understood than the function of these proteins in the cytoskeleton, but their presence in the nucleus is increasingly well documented, and our preliminary experiments show that 2,3-butanedione monoxime which is a relatively nonspecific inhibitor of myosin affects karyoplast rheology, as shown in Fig. S1 D. The possibility that actin filaments might contribute to karyoplast rheology is supported by earlier studies showing that the SWI/SNF complex contains a subunit of β-actin and an actin-related protein and nucleates actin filaments (64). Moreover, when actin polymerizes within the nucleus on a stiff substrate it is bound to the SWI/SNF complex, and this binding is essential for the transcriptional activity of YAP and TAZ regulators (63).

The current study has several limitations. The nuclei studied are only from fibroblasts, and only from cells in interphase, where the nucleus can be released intact by centrifugation. The data strongly suggest that the nucleus is not the stiffest organelle of the cell; internal membraneless organelles such as the nucleolus are stiffer (65) as are lipid droplets, even when their size is similar to that of the nucleus (13). Much remains to be learned about how nuclear composition relates to nuclear mechanics, and the method of making karyoplasts that retain much of the native structure and activities of the intact nucleus provides a useful tool for further studies.

#### **ACKNOWLEDGMENTS**

This work was supported by the US National Institutes of Health and the US National Science Foundation through grants NIH R35GM136259 and NSF

CMMI-1548571 (to P.A.J.) and NSF CMMI 2238600 and NIH R35GM142963 (to A.E.P.). G.J.L.W. thanks the BaSyC gravitation grant from NWO for funding. We are also grateful to Robert Bucki for help with osmotic stress experiments and for discussions with Qi Wen and Jay Tang.

# **AUTHOR CONTRIBUTIONS**

F.J.B., R.G.W., J.B., G.B., G.J.L.W., A.E.P., and P.A.J. designed the research. F.J.B., B.E., K.K.-L., K.M., D.L., W.C., and G.B. performed the research. F.J.B., B.E., R.G.W., J.B., G.B., G.J.L.W., A.E.P., and P.A.J. analyzed the data. F.J.B. and P.A.J. wrote the paper. K.M. contributed analytic tools.

#### **DECLARATION OF INTERESTS**

G.J.L.W. declares financial interest in LUMICKS.

#### **SUPPORTING MATERIAL**

Supporting material can be found online at https://doi.org/10.1016/j.bpj. 2024.11.3322.

#### **REFERENCES**

- 1. Cali, B., M. Deygas, , A. Viola. 2022. Atypical CXCL12 signaling enhances neutrophil migration by modulating nuclear deformability. Sci. Signal. 15:eabk2552. https://doi.org/10.1126/scisignal.abk2552.
- 2. Agsu, G., J. Gaillard, , M. Thery. 2022. Reconstituting the Interaction Between Purified Nuclei and Microtubule Network. Methods Mol. Biol. 2430:385-399. https://doi.org/10.1007/978-1-0716-1983-4 25
- 3. Niethammer, P. 2021. Components and Mechanisms of Nuclear Mechanotransduction. Annu. Rev. Cell Dev. Biol. 37:233-256. https:// doi.org/10.1146/annurev-cellbio-120319-030049.
- 4. Miroshnikova, Y. A., and S. A. Wickstrom. 2022. Mechanical Forces in Nuclear Organization. Cold Spring Harbor Perspect. Biol. 14:a039685. https://doi.org/10.1101/cshperspect.a039685.
- 5. Dahl, K. N., A. J. S. Ribeiro, and J. Lammerding. 2008. Nuclear shape, mechanics, and mechanotransduction. Circ. Res. 102:1307-1318. https://doi.org/10.1161/CIRCRESAHA.108.173989.
- 6. Zhu, J., Y. Tian, , X. Liu. 2022. The effects of measurement parameters on the cancerous cell nucleus characterisation by atomic force microscopy in vitro. J. Microsc. 287:3-18. https://doi.org/10.1111/
- 7. Wang, K., Y. Qin, and Y. Chen. 2021. In situ AFM detection of the stiffness of the in situ exposed cell nucleus. Biochim. Biophys. Acta Mol. Cell Res. 1868:118985. https://doi.org/10.1016/j.bbamcr.2021.118985.
- 8. Liu, H., J. Wen, , Y. Sun. 2014. In situ mechanical characterization of the cell nucleus by atomic force microscopy. ACS Nano. 8:3821–3828. https://doi.org/10.1021/nn500553z.
- 9. Wilhelm, C. 2008. Out-of-Equilibrium Microrheology inside Living Cells. Phys. Rev. Lett. 101:028101.
- 10. Bausch, A. R., W. Möller, and E. Sackmann. 1999. Measurement of Local Viscoelasticity and Forces in Living Cells by Magnetic Tweezers. Biophys. J. 76:573-579.
- 11. Wu, P.-H., D. R. B. Aroush, , D. Wirtz. 2018. A comparison of methods to assess cell mechanical properties. Nat. Methods. 15:491-498. https://doi.org/10.1038/s41592-018-0015-1.
- 12. Patteson, A. E., K. Pogoda, , P. A. Janmey. 2019. Loss of Vimentin Enhances Cell Motility through Small Confining Spaces. Small. 15:e1903180. https://doi.org/10.1002/sml1.201903180.

- 13. Loneker, A. E., F. Alisafaei, , R. G. Wells. 2023. Lipid droplets are intracellular mechanical stressors that impair hepatocyte function. Proc. Natl. Acad. Sci. USA. 120:e2216811120. https://doi.org/10. 1073/pnas.2216811120.
- 14. Ivanovska, I. L., M. P. Tobin, , D. E. Discher. 2023. Small lipid droplets are rigid enough to indent a nucleus, dilute the lamina, and cause rupture. J. Cell Biol. 222:e202208123. https://doi.org/10.1083/jcb. 202208123.
- 15. Rashid, F., S. A. Kabbo, and N. Wang. 2024. Mechanomemory of nucleoplasm and RNA polymerase II after chromatin stretching by a microinjected magnetic nanoparticle force. Cell Rep. 43:114462. https://doi.org/10.1016/j.celrep.2024.114462.
- 16. Goldman, R. D., R. Pollack, and N. H. Hopkins. 1973. Preservation of normal behavior by enucleated cells in culture. Proc. Natl. Acad. Sci. USA. 70:750–754. https://doi.org/10.1073/pnas.70.3.750.
- 17. Colonna, A., and S. J. Kerr. 1980. The nucleus as the site of tRNA methylation. J. Cell. Physiol. 103:29-33. https://doi.org/10.1002/jcp. 1041030105.
- 18. Ohara, J., T. Sekiguchi, and T. Watanabe. 1981. Purification of cytoplasts (enucleated cells) and karyoplasts (nuclei) from mouse splenic lymphocytes with cytochalasin-B. J. Immunol. Methods. 45:239-248. https://doi.org/10.1016/0022-1759(81)90302-1.
- 19. Pogoda, K., F. Byfield, , P. A. Janmey. 2022. Unique Role of Vimentin Networks in Compression Stiffening of Cells and Protection of Nuclei from Compressive Stress. Nano Lett. 22:4725-4732. https:// doi.org/10.1021/acs.nanolett.2c00736.
- 20. Mandal, K., D. Raz-Ben Aroush, , P. A. Janmey. 2019. Soft Hyaluronic Gels Promote Cell Spreading, Stress Fibers, Focal Adhesion, and Membrane Tension by Phosphoinositide Signaling, Not Traction Force. ACS Nano. 13:203-214. https://doi.org/10.1021/acsnano.8b05286.
- 21. Alisafaei, F., K. Mandal, , V. B. Shenoy. 2024. Vimentin is a key regulator of cell mechanosensing through opposite actions on actomyosin and microtubule networks. Commun. Biol. 7:658. https://doi.org/ 10.1038/s42003-024-06366-4.
- 22. Murrell, M. P., R. Voituriez, , M. L. Gardel. 2014. Liposome adhesion generates traction stress. Nat. Phys. 10:163-169. https://doi.org/ 10.1038/Nphys2855.
- 23. Goldman, R. D., R. Pollack, , A. Bushnell. 1975. Properties of enucleated cells. III. Changes in cytoplasmic architecture of enucleated BHK21 cells following trypsinization and replating. Exp. Cell Res. 93:175-183. https://doi.org/10.1016/0014-4827(75)90437-1.
- 24. Rodionov, V., E. Nadezhdina, , G. Borisy. 2001. Digital fluorescence microscopy of cell cytoplasts with and without the centrosome. Methods Cell Biol. 67:43-51. https://doi.org/10.1016/s0091-679x(01) 67004-3.
- 25. McMullen, A., M. Muñoz Basagoiti, , J. Brujic. 2022. Self-assembly of emulsion droplets through programmable folding. Nature. 610:502-506. https://doi.org/10.1038/s41586-022-05198-8.
- 26. McMullen, A., S. Hilgenfeldt, and J. Brujic. 2021. DNA self-organization controls valence in programmable colloid design. Proc. Natl. Acad. Sci. USA. 118:e2112604118. https://doi.org/10.1073/pnas. 2112604118.
- 27. Zhang, Y., A. McMullen, , P. M. Chaikin. 2017. Sequential self-assembly of DNA functionalized droplets. Nat. Commun. 8:21. https:// doi.org/10.1038/s41467-017-00070-0.
- 28. Brettschneider, J., J. M. Correnti, R. M. Carr , 2019. Rapid Lipid Droplet Isolation Protocol Using a Well-established Organelle Isolation Kit. J. Vis. Exp. 146:e59290. https://doi.org/10.3791/59290.
- 29. Lherbette, M., Á. Dos Santos, , I. A. T. Schaap. 2017. Atomic Force Microscopy micro-rheology reveals large structural inhomogeneities in single cell-nuclei. Sci. Rep. 7:8116. https://doi.org/10.1038/s41598-
- 30. Klymenko, O., J. Wiltowska-Zuber, , W. Kwiatek. 2009. Energy dissipation in the AFM elasticity measurements. Acta Phys. Pol. A. 115:548-551.

- Bergamaschi, G., A. S. Biebricher, G. J. L. Wuite. 2024. Heterogeneous force response of chromatin in isolated nuclei. *Cell Rep.* 43:114852. https://doi.org/10.1016/j.celrep.2024.114852.
- Patteson, A. E., A. Vahabikashi, P. A. Janmey. 2019. Vimentin protects cells against nuclear rupture and DNA damage during migration. J. Cell Biol. 218:4079–4092. https://doi.org/10.1083/jcb.201902046.
- Wu, Y., A. F. Pegoraro, , S. X. Sun. 2022. The correlation between cell and nucleus size is explained by an eukaryotic cell growth model. *PLoS Comput. Biol.* 18:e1009400. https://doi.org/10.1371/journal.pcbi. 1009400.
- Li, Z., B. Anvari, , W. E. Brownell. 2002. Membrane tether formation from outer hair cells with optical tweezers. *Biophys. J.* 82:1386–1395. https://doi.org/10.1016/S0006-3495(02)75493-3.
- 35. Pontes, B., N. B. Viana, H. M. Nussenzveig. 2011. Cell cytoskeleton and tether extraction. *Biophys. J.* 101:43–52. https://doi.org/10.1016/j.bpj.2011.05.044.
- Peeters, B. W. A., A. C. A. Piet, and M. Fornerod. 2022. Generating Membrane Curvature at the Nuclear Pore: A Lipid Point of View. *Cells*. 11:469. https://doi.org/10.3390/cells11030469.
- Kim, J., and Y. Okada. 1983. Asymmetric distribution and temperaturedependent clustering of filipin-sterol complexes in the nuclear membrane of Ehrlich ascites tumor cells. Eur. J. Cell Biol. 29:244–252.
- Govindaraju, M., H. S. Shekar, , A. J. Rajamma. 2013. Copper interactions with DNA of chromatin and its role in neurodegenerative disorders. *J. Pharm. Anal.* 3:354–359. https://doi.org/10.1016/j.jpha. 2013.03.003.
- Nguyen, T. H., K. L. Chen, and M. Elimelech. 2010. Adsorption kinetics and reversibility of linear plasmid DNA on silica surfaces: influence of alkaline earth and transition metal ions. *Biomacromolecules*. 11:1225–1230. https://doi.org/10.1021/bm901427n.
- Hardy, K. J., and S. E. Bryan. 1975. Localization and uptake of copper into chromatin. *Toxicol. Appl. Pharmacol.* 33:62–69. https://doi.org/10. 1016/0041-008X(75)90244-6.
- 41. Davidson, P. M., and J. Lammerding. 2014. Broken nuclei lamins, nuclear mechanics and disease. *Trends Cell Biol.* 24:247–256.
- Pfeifer, C. R., M. P. Tobin, D. E. Discher. 2022. Gaussian curvature dilutes the nuclear lamina, favoring nuclear rupture, especially at high strain rate. *Nucleus*. 13:129–143. https://doi.org/10.1080/19491034. 2022.2045726.
- Xia, Y., I. L. Ivanovska, D. E. Discher. 2018. Nuclear rupture at sites of high curvature compromises retention of DNA repair factors. J. Cell Biol. 217:3796–3808. https://doi.org/10.1083/jcb.201711161.
- Bieluszewski, T., S. Prakash, D. Wagner. 2023. The Role and Activity of SWI/SNF Chromatin Remodelers. *Annu. Rev. Plant Biol.* 74:139–163. https://doi.org/10.1146/annurev-arplant-102820-093218.
- Parry, B. R., I. V. Surovtsev, C. Jacobs-Wagner. 2014. The bacterial cytoplasm has glass-like properties and is fluidized by metabolic activity. Cell. 156:183–194. https://doi.org/10.1016/j.cell.2013.11.028.
- Janmey, P. A., and F. C. MacKintosh. 2014. Cytoplasmic transport: bacteria turn to glass unless kicked. *Curr. Biol.* 24:R226–R228. https://doi.org/10.1016/j.cub.2014.02.018.
- Guo, M., A. F. Pegoraro, D. A. Weitz. 2017. Cell volume change through water efflux impacts cell stiffness and stem cell fate. *Proc. Natl. Acad. Sci. USA*. 114:E8618–E8627. https://doi.org/10.1073/pnas.1705179114.
- Deviri, D., and S. A. Safran. 2022. Balance of osmotic pressures determines the nuclear-to-cytoplasmic volume ratio of the cell. *Proc. Natl. Acad. Sci. USA*. 119:e2118301119. https://doi.org/10.1073/pnas.2118301119.

- Lemiere, J., P. Real-Calderon, F. Chang. 2022. Control of nuclear size by osmotic forces in Schizosaccharomyces pombe. *Elife*. 11:e76075. https://doi.org/10.7554/eLife.76075.
- Goswami, R., A. Asnacios, , M. E. Chaboute. 2020. Mechanical Shielding in Plant Nuclei. *Curr. Biol.* 30:2013–2025.e3. https://doi. org/10.1016/j.cub.2020.03.059.
- Lammerding, J., L. G. Fong, not lamin B1 regulate nuclear mechanics. *J. Biol. Chem.* 281:25768– 25780. https://doi.org/10.1074/jbc.M513511200.
- Stephens, A. D., E. J. Banigan, J. F. Marko. 2017. Chromatin and lamin A determine two different mechanical response regimes of the cell nucleus. *Mol. Biol. Cell.* 28:1984–1996. https://doi.org/10.1091/ mbc.E16-09-0653.
- Pajerowski, J. D., K. N. Dahl, D. E. Discher. 2007. Physical plasticity of the nucleus in stem cell differentiation. *Proc. Natl. Acad. Sci. USA*. 104:15619–15624. https://doi.org/10.1073/pnas.0702576104.
- Denais, C. M., R. M. Gilbert, , J. Lammerding. 2016. Nuclear envelope rupture and repair during cancer cell migration. *Science*. 352:353–358. https://doi.org/10.1126/science.aad7297.
- Keizer, V. I. P., S. Grosse-Holz, , A. Coulon. 2022. Live-cell micromanipulation of a genomic locus reveals interphase chromatin mechanics. *Science*. 377:489–495. https://doi.org/10.1126/science.abi9810.ARTN.eabi9810.
- Sirinakis, G., C. R. Clapier, , Y. Zhang. 2011. The RSC chromatin remodelling ATPase translocates DNA with high force and small step size. EMBO J. 30:2364–2372. https://doi.org/10.1038/emboj.2011.141.
- Zhang, Y., C. L. Smith, C. Bustamante. 2006. DNA translocation and loop formation mechanism of chromatin remodeling by SWI/SNF and RSC. Mol. Cell. 24:559–568. https://doi.org/10.1016/j.molcel.2006.10.025.
- Imbalzano, K. M., N. Cohet, , J. A. Nickerson. 2013. Nuclear shape changes are induced by knockdown of the SWI/SNF ATPase BRG1 and are independent of cytoskeletal connections. *PLoS One.* 8:e55628. https://doi.org/10.1371/journal.pone.0055628.
- Imbalzano, A. N., K. M. Imbalzano, and J. A. Nickerson. 2013. BRG1, a SWI/SNF chromatin remodeling enzyme ATPase, is required for maintenance of nuclear shape and integrity. *Commun. Integr. Biol.* 6:e25153. https://doi.org/10.4161/cib.25153.
- Hargreaves, D. C. 2021. Chromatin openness requires continuous SWI/ SNF activity. Nat. Genet. 53:263–264. https://doi.org/10.1038/s41588-021-00781-7.
- Iurlaro, M., M. B. Stadler, D. Schübeler. 2021. Mammalian SWI/SNF continuously restores local accessibility to chromatin. *Nat. Genet.* 53:279–287. https://doi.org/10.1038/s41588-020-00768-w.
- 62. Schick, S., S. Grosche, , S. Kubicek. 2021. Acute BAF perturbation causes immediate changes in chromatin accessibility. *Nat. Genet.* 53:269–278. https://doi.org/10.1038/s41588-021-00777-3.
- Chang, L., L. Azzolin, , S. Piccolo. 2018. The SWI/SNF complex is a mechanoregulated inhibitor of YAP and TAZ. *Nature*. 563:265–269. https://doi.org/10.1038/s41586-018-0658-1.
- 64. Rando, O. J., K. Zhao, , G. R. Crabtree. 2002. Phosphatidylinositol-dependent actin filament binding by the SWI/SNF-like BAF chromatin remodeling complex. *Proc. Natl. Acad. Sci. USA*. 99:2824–2829. https://doi.org/10.1073/pnas.032662899.
- Louvet, E., A. Yoshida, , K. Takeyasu. 2014. Probing the stiffness of isolated nucleoli by atomic force microscopy. *Histochem. Cell Biol.* 141:365–381. https://doi.org/10.1007/s00418-013-1167-9.